Supplementary Figures

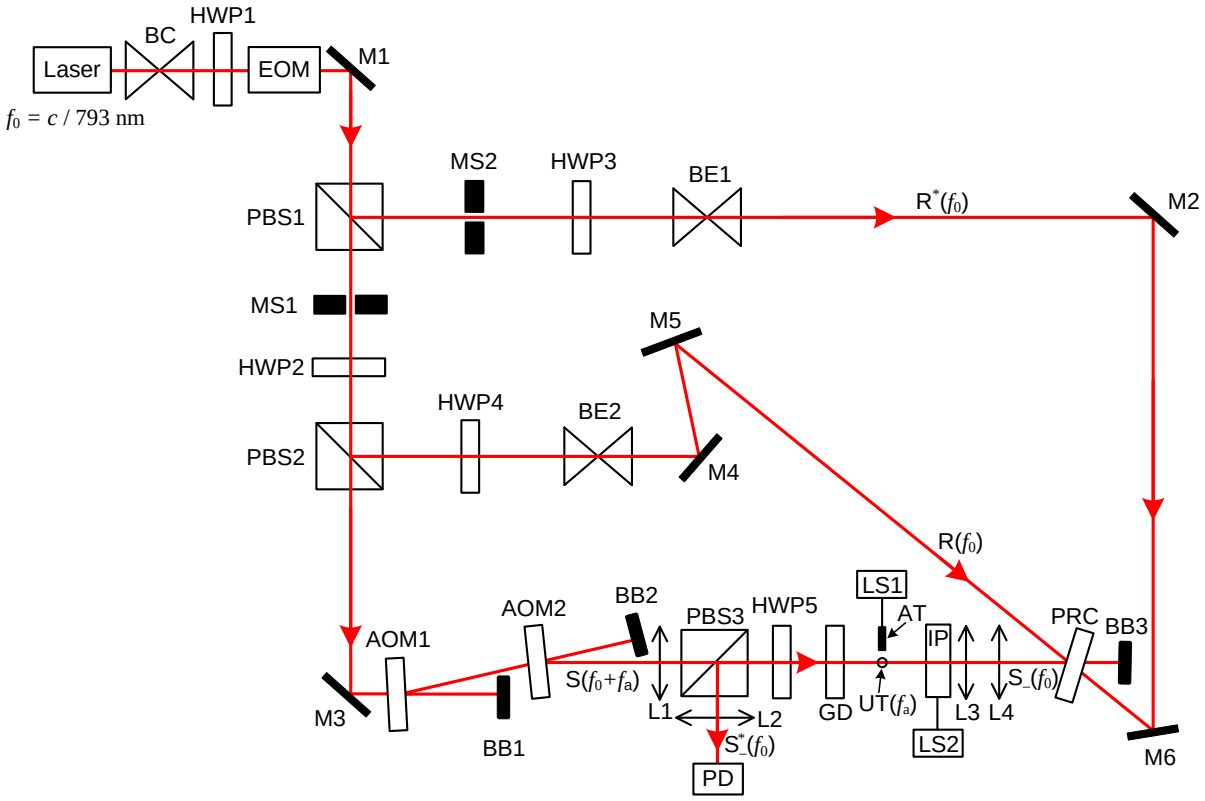

Supplementary Figure 1. Schematic of the experimental set-up for imaging an absorptive target inside a dynamic scattering medium with TRUE optical focusing. Abbreviations: AOM, acousto-optic modulator; AT, absorptive target; BB, beam block; BC, beam condenser; BE, beam expander; EOM, electro-optic modulator; f_0, frequency of the laser light; f_a, frequency detuning applied by AOMs, which was also the frequency used to drive the ultrasonic transducer; GD, ground glass diffuser; HWP, half-wave plate; IP, intralipid-gelatin phantom, mounted on a motorized linear stage; L, lenses; L3 & L4 were combined as L drawn in Fig. 2a, 2d of the main text, and were combined as L1 drawn in Fig. 2i and Fig. 3c of the main text; LS, linear stage; M, mirror; PBS, polarizing beamsplitter; PD, photodiode; PRC, photorefractive crystal; R, reference beam; R^*, reading beam, phase conjugate to R; S, sample light; S_-, frequency-down-shifted sample light (signal light); S^*_-, time-reversed signal light; MS, mechanical shutter; UT, ultrasonic transducer.

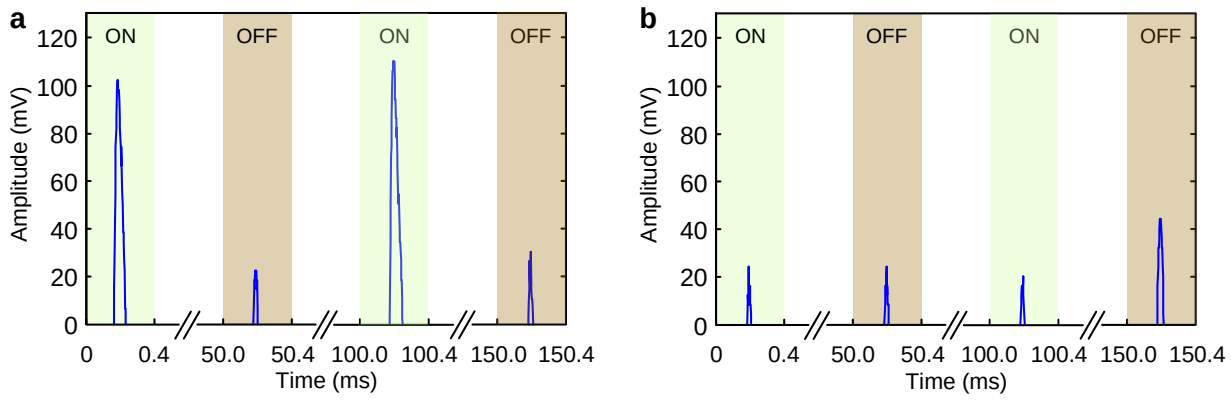

Supplementary Figure 2. Photodiode signal amplitudes of the detected S_{-}^{*} light diffracted from the holograms that were recorded when the focused ultrasonic modulation was on and off. The frequency of the focused ultrasonic modulation was 3.5 MHz (equal to the difference between the frequency of the light that illuminated the sample and the frequency of the reference beam) in (**a**), and shifted to 3.4 MHz in (**b**). A constant offset was subtracted in both figures.

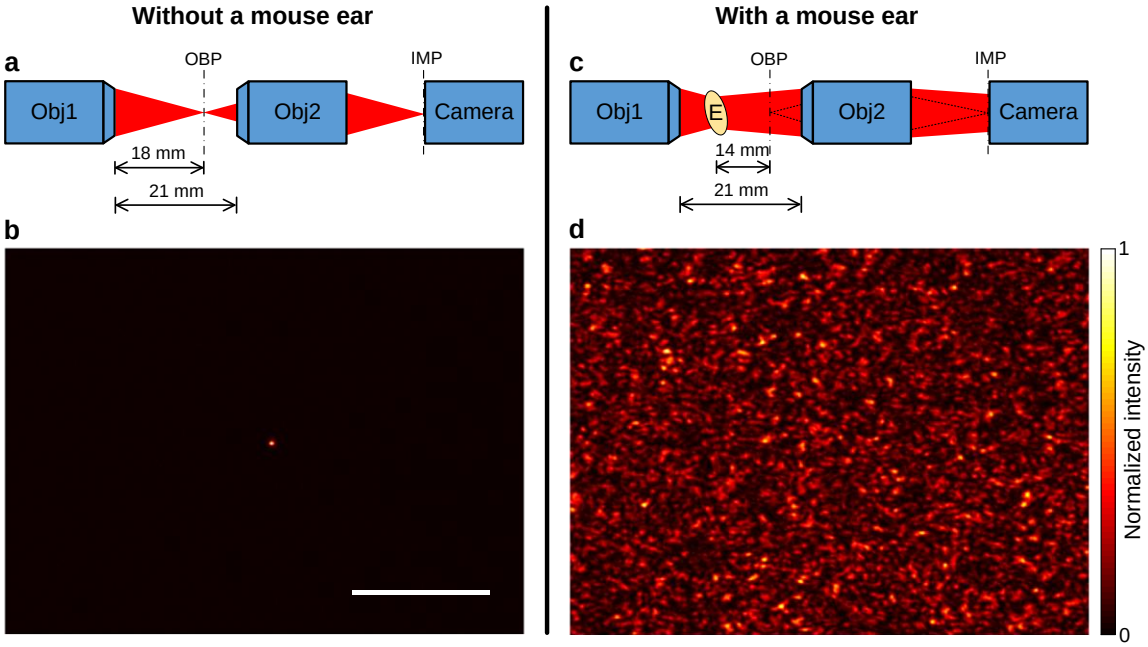

Supplementary Figure 3. Light intensity distributions on the focal plane of an objective (Obj1) before and after a living-mouse ear was inserted as a scattering medium. (**a**) The experimental set-up. The focal plane of objective 1 (AC080-020-B-ML, Thorlabs Inc., USA. Working distance = 18 mm, NA = 0.2) was imaged by objective 2 (Leica, E1 ACHRO, 10×, NA = 0.25) and a CMOS camera (FMVU-03MTM, Point Grey, Canada). (**b**) The light intensity distribution on the focal plane of objective 1. The full width at half maximum focal spot size was 2.4 μm on the object plane, which was close to the diffraction-limited focal spot size (2.0 μm). (**c**) A living-mouse ear (E) was inserted between objective 1 and its focal plane. The distance between the mouse ear and the focal plane was 14 mm, which was the same as the distance between the mouse ear and the ultrasonic focus in the TRUE focusing experiment illustrated in Fig. 3c. (**d**) The light intensity distribution on the focal plane of objective 1. The focus in (**b**) could no longer be observed due to scattering of the mouse ear. Abbreviations: E, mouse ear; IMP, image plane; Obj, objective; OBP, object plane. Scale bar, 1 mm.

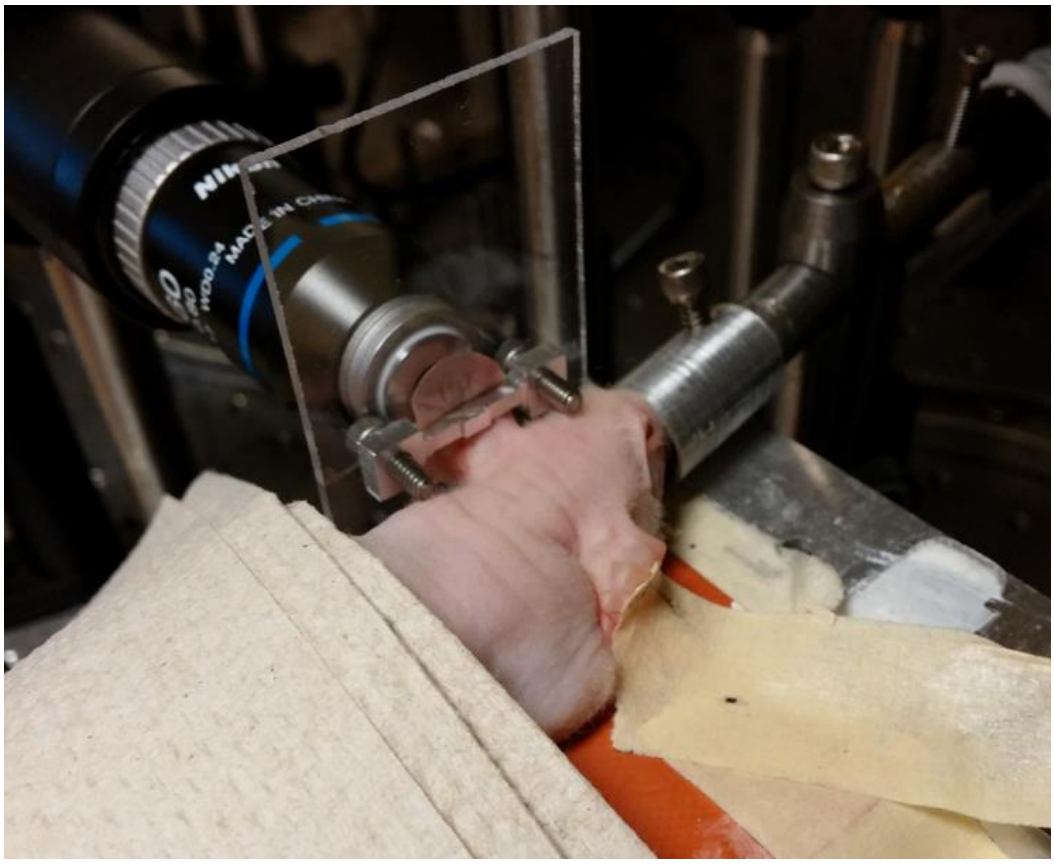

Supplementary Figure 4. A photo of the set-up used to measure the speckle correlation time after blocking the blood flow in the mouse ear. A metal bar pressed the ear against a stiff acrylic wall to block its blood flow.

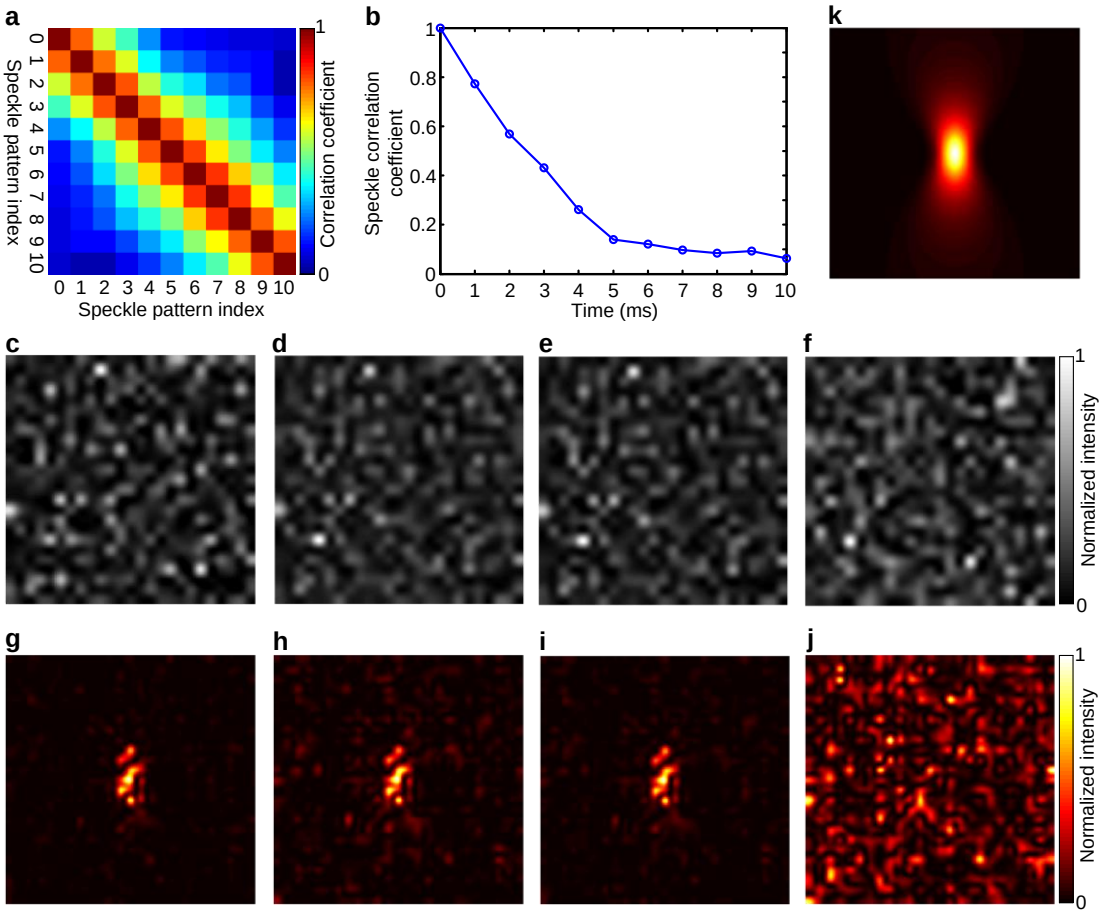

Supplementary Figure 5. Simulation of TRUE optical focusing inside a dynamic scattering medium with a speckle correlation time of 5.2 ms. (**a**) The correlation coefficients between different speckle patterns. The i^{th} speckle pattern is the speckle pattern on the PRC (formed by signal light S_-) at the time of i ms. (**b**) The correlation coefficients between the speckle pattern at 0 ms, and each of the ensuing speckle patterns, from which τ_c = 5.2 ms was determined. (**c**) The correct hologram formed by the interference between S_- and the reference beam R at 10 ms. The partially blurred hologram within the hologram writing time (10 ms) (**d**) can be decomposed into a partially blurred hologram within τ_c ((**e**), formed by the integration of the interference patterns between the S_- and R at 5 – 10 ms) and an incorrect hologram ((**f**), formed by the integration of the interference patterns between S_- and R at 0 – 4 ms). (**g–j**) The light intensity distributions on Plane A (i.e., the *x*-*z* plane intersecting the acoustic axis in Fig. 1a) when the corresponding holograms in (**c**−**f**) were read. (**k**) The ultrasonic modulation efficiency distribution. All the images were normalized by their own maximum values.

Supplementary Notes

Supplementary Note 1: The required number of independent control elements increases quadratically with focusing depth.

In wavefront shaping, the focusing efficiency η is defined as the ratio of the energy deposited at the targeted location (where a guide star is placed) to that reflected by a SLM (with pixel number *N*). Due to reciprocity[1], the efficiency is equal to the ratio of the number of optical modes on the SLM to the total number of output modes that emanate from the guide star. The total number of optical modes, N_{Total}, can be estimated by $N_{\text{Total}} = 4\pi l^2 / (\lambda/2)^2$, where l is the depth of the targeted location and λ is the wavelength of the laser light in the scattering medium; $\lambda/2$ is the approximated speckle size. So, $\eta = (N/4)/N_{\text{Total}} = N/\left[16\pi l^2/(\lambda/2)^2\right]$, which is proportional to N/l^2. Thus, in order to keep the focusing efficiency, the number of independent control elements N should increase quadratically with focusing depth l.

It should be noted that the above conclusion does not hold if we consider from the perspective of focusing quality. The focusing quality, in terms of peak to background ratio[2] (PBR), can be calculated by π (*N*+1)/(4*M*), where *M* is the number of modes in the focus. $M = d_x \times d_y / d^2$, where d_x, d_y are the dimensions of the focus perpendicular to the optical axis *z*, and *d* is the speckle size. If we focus light inside scattering media beyond a certain depth (denoted as *L*) where speckle is fully developed, the speckle size can be approximated as $\lambda/2$ and it no longer decreases with depth, so the PBR will stay unchanged beyond *L*.

Supplementary Note 2: Remarks on the speckle patterns (shown in Supplementary Movie 1a) formed by light passing through a living-mouse ear.

The light intensity at each position on the camera has contributions from both blood-scattered photons and non-blood-scattered photons. So, the output of each pixel of the camera, $V(\vec{r},t)$, can be expressed as:

$$V(\vec{r},t) \propto \int_{t-T/2}^{t+T/2} \left|E(\vec{r},\tau)\right|^2 d\tau = \int_{t-T/2}^{t+T/2} \left|\tilde{E}_{\mathrm{s}}(\vec{r})\exp(-i\omega\tau) + \tilde{E}_{\mathrm{d}}(\vec{r},\tau)\exp(-i\omega\tau)\right|^2 d\tau .$$

Here, $\tilde{E}_{\mathrm{s}}(\vec{r})$ is the complex amplitude of the net electric field (E-field) of non-blood-scattered light at position $\vec{r}$, which does not change over time; $\tilde{E}_{\mathrm{d}}(\vec{r},\tau)$ is the complex amplitude of the net E-field of blood-scattered light at position $\vec{r}$ and time τ; ω is the frequency of the laser light; and T is the camera's exposure time. The intensities of the bright speckle grains in the seemingly-static background pattern fluctuate over time at small amplitudes, which can be explained as follows. In these speckle grains, the phasor $\tilde{E}(\vec{r},t) = \tilde{E}_{\mathrm{s}}(\vec{r}) + \tilde{E}_{\mathrm{d}}(\vec{r},t)$ is a vector sum of a large constant vector in the complex plane and a small vector which rotates randomly over time and changes its length. Since $\left|\tilde{E}_{\mathrm{s}}(\vec{r})\right|$ is much larger than $\left|\tilde{E}_{\mathrm{d}}(\vec{r},t)\right|$, the resulting amplitude of the phasor $\tilde{E}(\vec{r},t)$ can be approximated by $\left|\tilde{E}_{\mathrm{s}}(\vec{r})\right|$, thus the intensity $I(\vec{r},t)$ appears to be constant in these speckle grains.

Supplementary Note 3: Simulation of TRUE optical focusing inside a dynamic scattering medium with a speckle correlation time of 5.6 ms.

Similar to the procedures described in Methods, the E-field of the ultrasonically encoded light on the PRC can be calculated by $\mathbf{b} = \mathbf{Ta}$, where **T** is the transmission matrix (dimension = 625×625) and **a** is the ultrasonically encoded light field (dimension = 625×1) on the *x*-*z* plane intersecting the acoustic axis (denoted as plane A, see Fig. 1a). In our phantom experiment, since the speckle pattern $|\mathbf{b}|^2$ had a speckle correlation time (τ_c) of 5.6 ms when the phantom was moved at 0.100 mm/s, we simulated 11 transmission matrices $\mathbf{T_i}$ (i = 0, 1, 2,⋯, 10, representing the scattering medium at the time of i ms), whose elements $[\mathbf{T_i}]_{jk}$ were correlated because they were sampled from 9-point moving averaging of a sequence of random complex numbers. Specifically, $[\mathbf{T_i}]_{jk} = \sum_{p=i-4}^{p=i+4} [\mathbf{M_p}]_{jk} / 9$ (i = 0, 1, 2,⋯, 10), where $\mathbf{M_p}$ (p = −4, −3, ⋯, 14) are 19 independent random matrices whose elements follow the circular Gaussian distribution, and $\mathbf{M_p}\mathbf{M_p}^{\dagger} \approx \hat{\mathbf{I}}$, where "†" denotes conjugate transpose and $\hat{\mathbf{I}}$ is the identity matrix. The speckles at different time, $\mathbf{b_i} = \mathbf{T_i a}$, were correlated with a τ_c = 5.2 ms (see Supplementary Fig. 5a–5b), similar to the measured value (τ_c = 5.6 ms) in our experiments. $\mathbf{b_i}$ interfered with a reference beam R (whose E-field was represented by a vector **R** (dimension = 625×1) in which all elements were 1) and formed an interference pattern $\mathbf{I_i} = |\mathbf{b_i} + \mathbf{R}|^2$. The hologram recorded within the writing time (t_w = 10 ms) was proportional to a weighted summation of $\mathbf{I_i}$ (see Supplementary Fig. 5d) as in:

$$\mathbf{h_{t_w}} = \mathbf{h}(t = t_w = 10 \text{ ms}) \propto \int_0^{t=10 \text{ ms}} \mathbf{I}(t-\tau) \exp(-\tau / \tau_r) \, d\tau \approx \sum_{i=0}^{10} |\mathbf{b_i} + \mathbf{R}|^2 \, w_i,$$

$$w_i = \exp\left[-(10-i)/\tau_r\right].$$

Here, τ_r = 7 ms is the response time of the PRC at 1 W cm^{-2}. If the response time of the PRC was much shorter than τ_c, $\mathbf{h}(t = 10\text{ ms}) \triangleq \mathbf{h_{Correct}} \propto \mathbf{I_{10}}$ (see Supplementary Fig. 5c). It can be seen that although $\mathbf{h}_{t_w}$ was partially blurred compared with $\mathbf{h_{Correct}}$, it was still highly correlated with $\mathbf{h_{Correct}}$ (r = 0.74). $\mathbf{h}_{t_w}$ could be further decomposed into $\mathbf{h}_{\tau_c}$ and $\mathbf{h_{Wrong}}$. $\mathbf{h}_{\tau_c} \propto \sum_{i=5}^{10} \left|\mathbf{b_i} + \mathbf{R}\right|^2 w_i$ was the hologram integrated over a duration of τ_c starting at time $t_w - \tau_c$. Compared with $\mathbf{h}_{t_w}$, $\mathbf{h}_{\tau_c}$ was expected to resemble $\mathbf{h_{Correct}}$ more closely due to reduced blurring (r = 0.81, see Supplementary Fig. 5e). $\mathbf{h_{Wrong}} \propto \sum_{i=0}^{4} \left|\mathbf{b_i} + \mathbf{R}\right|^2 w_i$ was the hologram integrated from time 0 to $t_w - \tau_c$. Since $\mathbf{b_i}$ (i = 0 – 4) was poorly correlated with $\mathbf{b_{10}}$, $\mathbf{h_{Wrong}}$ was expected to be poorly correlated with $\mathbf{h_{Correct}}$ (r = 0.12, see Supplementary Fig. 5f).

In the time-reversal step, the hologram $\mathbf{h}_{t_w}$ was read by a reading beam R* (whose E-field was represented by a vector $\mathbf{R}^*$) at t = 10 ms, and the −1st order diffracted light was generated, which was proportional to $\sum_{i=0}^{10} \mathbf{b_i^*} w_i$. At this time, the dynamic scattering medium (i.e. the intralipid-gelatin phantom) was represented by the transmission matrix $\mathbf{T_{10}}$, and the light field distribution on plane A in Fig. 1a, $\mathbf{a}_{t_w}^*$, was proportional to $\mathbf{T_{10}}^T \sum_{i=0}^{10} \mathbf{b_i^*} w_i$ (see Supplementary Fig. 5h for the intensity distribution $\left|\mathbf{a}_{t_w}^*\right|^2$), where the superscript "T" denotes matrix transpose. If $\mathbf{h_{Correct}}$ was read, the field distribution on plane A, $\mathbf{a}_{\mathbf{Correct}}^*$, was proportional to $\mathbf{T_{10}}^T \mathbf{b_{10}^*} \approx \mathbf{a}^*$

(assuming $\mathbf{T_{10}}^{\dagger}\mathbf{T_{10}} \approx \hat{\mathbf{I}}$), representing the ideal TRUE focus (see Supplementary Fig. 5g for $\left|\mathbf{a}^{*}_{\mathbf{Correct}}\right|^2$). The background in $\left|\mathbf{a}^{*}_{\mathbf{Correct}}\right|^2$ was due to partial time-reversal[2] (i.e. not all the output modes were detected and time-reversed). Compared with $\left|\mathbf{a}^{*}_{\mathbf{Correct}}\right|^2$, there was a stronger background in $\left|\mathbf{a}^{*}_{\mathbf{t_w}}\right|^2$. This elevated background could be better understood by studying the readout of the hologram $\mathbf{h}_{\boldsymbol{\tau_c}}$ and $\mathbf{h}_{\mathbf{Wrong}}$ ($\mathbf{h}_{\mathbf{t_w}} = \mathbf{h}_{\boldsymbol{\tau_c}} + \mathbf{h}_{\mathbf{Wrong}}$), simulated by $\mathbf{a}^{*}_{\boldsymbol{\tau_c}} \propto \mathbf{T_{10}}^{T} \sum_{i=5}^{10} \mathbf{b}^{*}_{\mathbf{i}} w_i$ and $\mathbf{a}^{*}_{\mathbf{Wrong}}$ $\propto \mathbf{T_{10}}^{T} \sum_{i=0}^{4} \mathbf{b}^{*}_{\mathbf{i}} w_i$, respectively (see Supplementary Fig. 5i−5j for the intensity distributions $\left|\mathbf{a}^{*}_{\boldsymbol{\tau_c}}\right|^2$ and $\left|\mathbf{a}^{*}_{\mathbf{Wrong}}\right|^2$). It can be seen that the little-blurred hologram $\mathbf{h}_{\boldsymbol{\tau_c}}$ generated a TRUE focus with good fidelity, while the incorrect hologram $\mathbf{h}_{\mathbf{Wrong}}$ generated a background $\left|\mathbf{a}^{*}_{\mathbf{Wrong}}\right|^2$ with no focus. For the background $\left|\mathbf{a}^{*}_{\mathbf{Wrong}}\right|^2$, the energy of light was broadly distributed in space so that the intensity at each position was much lower than the intensity in the TRUE focus in $\left|\mathbf{a}^{*}_{\boldsymbol{\tau_c}}\right|^2$. Because of this, the background in $\left|\mathbf{a}^{*}_{\mathbf{t_w}}\right|^2$ is only slightly stronger than the background in $\left|\mathbf{a}^{*}_{\mathbf{Correct}}\right|^2$, and thus the quality of the TRUE focus in $\left|\mathbf{a}^{*}_{\mathbf{t_w}}\right|^2$ is comparable with that in $\left|\mathbf{a}^{*}_{\mathbf{Correct}}\right|^2$ (r = 0.93).

References

1. McMichael, I., Ewbank, M.D. & Vachss, F. Efficiency of phase conjugation for highly scattered light. *Opt. Commun.* **119**, 13-16 (1995).
2. Wang, Y.M., Judkewitz, B., DiMarzio, C.A. & Yang, C. Deep-tissue focal fluorescence imaging with digitally time-reversed ultrasound-encoded light. *Nat. Commun.* **3**, 928 (2012).